Radio Point Sources Toward Galaxy Clusters at 30 GHz

K. Coble[1,2,3], J. E. Carlstrom[3,4], M. Bonamente[5,6], K. Dawson[7], W. Holzapfel[7], M. Joy[5], S. LaRoque[3], E. D. Reese[8]

ABSTRACT

Extra-galactic point sources are a significant contaminant in cosmic microwave background and Sunyaev-Zel'dovich effect experiments. Deep interferometric observations with the BIMA and OVRO arrays are used to characterize the spatial, spectral, and flux distributions of radio point sources toward galaxy clusters at 28.5 GHz. We compute counts of mJy point source fluxes from 90 fields centered on known massive galaxy clusters and 8 non-cluster fields. We find that source counts in the inner regions of the cluster fields (within 0.5 arcmin of the cluster center) are a factor of $8.9^{+4.3}_{-2.8}$ times higher than counts in the outer regions of the cluster fields (radius greater than 0.5 arcmin). Counts in the outer regions of the cluster fields are in turn a factor of $3.3^{+4.1}_{-1.8}$ greater than those in the non-cluster fields. Counts in the non-cluster fields are consistent with extrapolations from the results of other surveys. We also compute source counts toward clusters as a function of luminosity in three redshift bins out to $z = 1.0$ and see no clear evidence for evolution with redshift. We compute spectral indices of mJy sources in cluster fields between 1.4 and 28.5 GHz and find a mean spectral index of $\alpha = 0.70$ with an rms dispersion of 0.34, where flux $S \propto \nu^{-\alpha}$. The distribution is skewed, with a median spectral index of 0.76 and 25th and 75th percentiles of 0.55 and 0.95, respectively. This is steeper than the spectral indices of brighter field point sources measured by other surveys.

[1]Dept. of Chemistry and Physics, Chicago State University, 9501 South King Drive, Chicago, IL 60628, coble@hyde.uchicago.edu

[2]NSF Astronomy and Astrophysics Postdoctoral Fellow, Adler Planetarium and Astronomy Museum

[3]Dept. of Astronomy and Astrophysics, Kavli Institute for Cosmological Physics, University of Chicago, 5640 South Ellis Ave., Chicago, IL 60637

[4]Dept. of Physics, Enrico Fermi Inst., University of Chicago, 5640 South Ellis Ave., Chicago, IL 60637

[5]Dept. of Space Science - NSSTC, NASA Marshall Space Flight Center, Huntsville, AL 35812

[6]Dept. of Physics, University of Alabama in Huntsville, Huntsville, AL 35805

[7]Dept. of Physics, University of California, Berkeley, CA 94720, (KD now at LBNL)

[8]Physics Department, University of California, Davis, CA

Subject headings: galaxies: clusters — cosmology: observations — cosmic microwave background — radio continuum: galaxies

1. INTRODUCTION

Extra-galactic point sources are a significant contaminant in cosmic microwave background (CMB) and Sunyaev-Zel'dovich effect (SZE) experiments (Holder 2002; Knox et al. 2004; Tegmark et al. 2000). Measurements of the cosmic microwave background and of the Sunyaev-Zel'dovich effect (Sunyaev & Zel'dovich 1970, 1972) have the potential to yield a wealth of cosmological information if foreground contaminants are well-understood.

Point sources are often associated with the clusters themselves. This is a potential source of bias for current and planned SZE surveys such as the Sunyaev-Zel'dovich Array (SZA)[1], Arcminute Microkelvin Imager (AMI)[2], the Atacama Pathfinder Experiment Sunyaev-Zel'dovich (APEX-SZ) survey[3], the South Pole Telescope (SPT)[4], and the the Atacama Cosmology Telescope (ACT)[5]. To understand the impact on planned SZE cluster surveys, it is critical to completely characterize the spatial, spectral, and flux distribution of point sources associated with clusters.

Extra-galactic point sources come in two basic varieties: radio point sources, which are powered by active galactic nuclei (AGN) and dominate at lower frequencies and dusty galaxies, which dominate at higher frequencies. At our observing frequency of 28.5 GHz, radio point sources dominate. Models for the number counts of radio point sources as a function of flux (Toffolatti et al. 1999; Sokasian et al. 2001) have been derived from observations at lower frequencies and extrapolated to microwave frequencies.

Several CMB experiments, such as WMAP (Bennett et al. 2003), DASI (Kovac et al. 2002), VSA (Cleary et al. 2005), and CBI (Mason et al. 2003), have measured cm-wave source counts as a function of flux for sources brighter than about 10 mJy. There have been two prior analyses of point sources in SZE data taken with the Owens Valley Radio Observatory

[1]SZA website: http://astro.uchicago.edu/ sza

[2]AMI website: http://www.mrao.cam.ac.uk/telescopes/ami/

[3]APEX-SZ website: http://bolo.berkeley.edu/apexsz

[4]SPT website: http://spt.uchicago.edu/

[5]ACT website: http://www.hep.upenn.edu/act/

(OVRO)[6] and Berkeley-Illinois-Maryland Association (BIMA)[7] arrays. Using a sample of 56 fields centered on known massive galaxy clusters, Cooray et al. (1998) computed counts and spectral indices of point sources. Using the outer regions of 41 cluster fields, LaRoque et al. (2002) computed the normalization of source counts as a function of flux for faint point sources in SZE data. The data used in Cooray et al. (1998) and in LaRoque et al. (2002) are subsets of the data presented in this paper.

In this paper, we characterize the spatial, spectral, and flux distribution of faint ($\sim$ mJy) radio point sources from data obtained at the BIMA and OVRO arrays at 28.5 GHz, using 90 fields centered on known massive galaxy clusters and 8 non-cluster fields. We also investigate the redshift dependence of source counts as a function of luminosity. Section 2 describes the observations, data reduction, and field selection. Section 3 presents the measured point source fluxes and the methods used to obtain them. In Section 4, we compute spectral indices between 1.4 and 28.5 GHz using fluxes from our data and from NVSS and other surveys. In Section 5, we present source counts as a function of flux for cluster and non-cluster fields as well as the redshift and angular dependence of counts in cluster fields. We compare our results with those from other experiments and with theoretical models.

2. OBSERVATIONS

2.1. Observations

The 28.5 GHz observations were carried out with the Berkeley Illinois Maryland Association millimeter array (BIMA) during the summers of 1996 – 2002 and the Owens Valley Radio Observatory (OVRO) during the summers of 1995 – 2001 as part of the OVRO/BIMA SZE imaging project (see, for example, Reese et al. (2002) and Grego et al. (2001)). A total of 63 cluster fields were observed at BIMA and 54 cluster fields were observed at OVRO. 27 of the cluster fields were observed at both BIMA and OVRO, yielding observations of 90 unique cluster fields. For the BIMA CMB project (Dawson et al. 2002, 2006), a total of 18 non-cluster fields were observed.

The BIMA array consists of ten 6.1 meter diameter telescopes with primary beams of 6.6 arcmin FWHM; nine of the ten BIMA telescopes were used for the 30 GHz observations. The OVRO array consists of six 10.4-meter telescopes, with primary beams of 4.2 arcmin FWHM; all six OVRO telescopes were used for the 30 GHz observations. The primary beams were

[6]The OVRO mm-wave array is operated by Caltech with support from the National Science Foundation

[7]The BIMA array is operated with support from the National Science Foundation

measured with holography and were found to be well-approximated by Gaussians; we use the azimuthally averaged measured beam responses in our analyses. For CMB observations at BIMA, the array was set in a compact configuration to maximize brightness sensitivity. For cluster observations at both OVRO and BIMA, some telescopes are placed at longer baselines for point source monitoring.

The telescopes were outfitted with cm-wave receivers (Carlstrom et al. 1996) equipped with cryogenically cooled 26 - 36 GHz HEMT amplifiers (Pospieszalski et al. 1995). Typical receiver temperatures were 11 K to 20 K, and when integrated with the OVRO and BIMA telescopes yielded typical system temperatures scaled to above the atmosphere of 45 K to 55 K, and as low as 35 K. OVRO observations employed two 1 GHz bandwidth channels centered at 28.5 and 30 GHz. BIMA observations were made with an 0.8 GHz bandwidth centered at 28.5 GHz.

Observations of cluster and CMB fields were interleaved every ~ 20 minutes with observations of a bright point source for phase calibration. Observations of the phase calibrators indicate gain variations of $\sim 1\%$ over several months. The absolute calibration is based on observations of Mars, with the brightness temperature taken from the Rudy (1987) model. Further details of the observations and the data reduction can be found in Grego et al. (2001) and Reese et al. (2002).

2.2. Field Selection

The cluster fields of the full OVRO/BIMA SZE imaging project were chosen to obtain precise measurements of the SZE in massive galaxy clusters. Potential targets were screened for extremely bright radio sources using archival data at lower frequencies such as NVSS (Condon et al. 1998) and FIRST (White et al. 1997). In addition, if a bright point source ($> 10 - 20$ mJy) was detected near the cluster center in the initial 28.5 GHz observations, observations ceased in favor of other less contaminated targets. Due to the constraints of this field selection, we do not attempt to characterize the distribution of point sources brighter than 10 mJy in this analysis.

The cluster fields were chosen from an assortment of X-ray and optical catalogs, including: (1) the ROSAT Brightest Cluster Survey, BCS (Ebeling et al. 1997, 1998, 2000a; Crawford et al. 1999), (2) the Einstein Observatory Extended Medium Sensitivity Survey, EMSS (Gioia et al. 1990; Stocke et al. 1991; Gioia & Luppino 1994; Maccacaro et al. 1994), (3) the ROSAT X-ray Brightest Abell Clusters, XBACS (Ebeling et al. 1996b,a), (4) the Wide Angle ROSAT Pointed Survey, WARPS (Scharf et al. 1997; Jones et al. 1998; Fairley

et al. 2000; Ebeling et al. 2000b), (5) the Massive Cluster Survey, MACS (Ebeling et al. 2001a), and (6) the Red-Sequence Cluster Survey, RCS (Gladders & Yee 2005).

Clusters were selected from the BCS, EMSS, and XBACS X-ray catalogs on the basis of high X-ray luminosity. Clusters from the WARPS and MACS surveys were selected for X-ray luminosity and high redshift. The 8 clusters selected for SZE observations from the MACS survey form a complete redshift-selected flux-limited X-ray sample and were chosen regardless of possible point source contamination. A few optically selected clusters were also provided by the RCS team.

Table 1 lists the cluster fields, the coordinates of the field pointing centers, the relative offset of the best fit central decrement, and the cluster redshift. Determinations of the SZE centroids are typically better than 10 arcsec.

Table 2 lists the non-cluster fields and the coordinates of their pointing centers. Of the 18 fields observed as part of the BIMA CMB project, only the 8 fields BDF14-BDF21 (Dawson et al. 2006) were chosen without regard to possible point source contamination. The fields BDF4, and BDF6-BDF13 (Dawson et al. 2002) were chosen from the NVSS survey to have minimal contamination from strong point sources. The field HDF is centered on the Hubble Deep Field and was also selected to have no bright radio sources. Only the 8 fields selected without regard to point source contamination are used in the analysis presented in this paper.

3. POINT SOURCE FLUXES

Point source fluxes and cluster parameters are first estimated using the DIFMAP software package (Pearson et al. 1994). The SZE data consist of positions in the Fourier domain (also called the $u-v$ plane) and the visibilities—the complex Fourier component pairs as functions of u and v, which are the Fourier conjugate variables to right ascension and declination. DIFMAP is used to create a map from the $u-v$ data using all baselines and natural weighting ($\propto \sigma^{-2}$). Point sources with flux above a threshold of five times the image RMS are identified and removed from the visibility data one at a time using the CLEAN algorithm. The cluster SZE decrement (if any) is removed by fitting in the $u-v$ plane to the Fourier transform of an isothermal, elliptical β model. The residual map, made from all baselines with no taper, is searched for additional point sources. Noise estimates are then extracted from the images.

The estimates of the source positions are then used as the starting point for a maximum likelihood joint analysis, which simultaneously models the SZE cluster emission along with

any point sources in the field. The modeling is performed in the $u - v$ plane, which is the natural form of the data where the noise properties and spatial filtering of the interferometer are well understood. Galaxy clusters are modeled with a spherical isothermal β-model (Cavaliere & Fusco-Femiano 1976, 1978). Details of the modeling can be found in Reese et al. (2002, 2000). For the cluster fields with no detected decrement and for non-cluster fields, we do not include a SZ decrement model in the fits. We correct the fluxes of all point sources for attenuation from the primary beam.

We measure the noise levels from maps made with all baselines which have had all point sources and the SZE decrement removed. Typical rms noise levels are 0.14 mJy for the BIMA cluster fields, 0.08 mJy for the OVRO cluster fields, and 0.08 mJy for the BIMA non-cluster fields. Some of the cluster fields have a lower integration time, and thus a much higher noise level, up to 0.85 mJy. The heterogeneous noise levels of the cluster fields are due to the heterogeneous selection of fields described in Section 2.2; fields with bright central sources were not observed for long because they were not ideal targets for measuring the SZE.

Table 1 lists the beam-corrected 28.5 GHz fluxes for point sources detected in the BIMA and OVRO cluster fields. Noise levels for each field, the S/N ratio for each source, the position of each source with respect to the field center, the beam attenuation factor at that position, and the SZE decrement centroid (if detected) with respect to the field center are also given. At the 5σ-level or greater, we detect 60 point sources in the 63 BIMA cluster fields and 54 point sources in the 54 OVRO cluster fields. A total of 23 sources are detected at both BIMA and OVRO, yielding 91 unique sources in the 90 cluster fields. For sources observed at both BIMA and OVRO, the flux measurements are in good agreement. Point source fluxes, positions, and noise levels for the non-cluster fields are given in Table 2. We detect two point sources at $\geq 5\sigma$ in the 8 BIMA non-cluster fields which were selected without regard to possible point source contamination.

4. SPECTRAL INDICES

We use the results of surveys at lower observing frequency to constrain the spectral indices of point sources detected with the BIMA/OVRO observations. Fluxes at 1.4 GHz are taken primarily from the NVSS catalog, which has a resolution of 45 arcsec and limiting peak source brightness of 2.5 mJy. We obtain 1.4 GHz fluxes from the FIRST catalog (limiting flux of 1 mJy and resolution of 5 arcseconds) for several additional sources which were below the NVSS detection threshold. We obtain 1.4 GHz fluxes from VLA archival maps for several sources which were not in the NVSS or FIRST catalogs. Of the 91 sources in cluster fields, 87 of them have unambiguous counterparts in the NVSS, FIRST, or VLA

archival data. All central cluster point sources found in the NVSS fields were confirmed to have counterparts at 28.5 GHz. The 1.4 GHz fluxes and the results of a literature search for low frequency measurements of sources not identified in the NVSS, FIRST, or VLA surveys are given in Table 1. Unless otherwise noted, the tabulated 1.4 GHz fluxes are from NVSS. For the 4 sources that do not have unambiguous 1.4 GHz counterparts in NVSS, FIRST, or the VLA archive, we assume a 1.4 GHz flux equal to three times the survey noise. In reality, the true 1.4 GHz fluxes must be less and the true spectral indices of these sources more shallow. However, because there are only four sources lacking 1.4 GHz detections, the bias in the resulting mean spectral index for all point sources in cluster fields computed below is small. Furthermore, because the 1.4 and 28.5 GHz measurements were not made contemporaneously, variability of the sources may contribute to a broadening in the distribution of spectral indices.

A subsample of 24 clusters was observed using the VLA[8] at a frequency of 4.8 GHz between the years 2001 and 2002. A total of 25 point sources from the OVRO/BIMA surveys were identified in maps at a resolution of $4''$ for fields observed in the compact D configuration and at $1.5''$ for fields observed in the extended A,B,C configurations. The 4.8 GHz fluxes found in Table 1 are determined using the CLEAN algorithm in a $8'' \times 8''$ box centered on the brightest pixel. Sources are detected and removed one at a time to a detection threshold of 0.30 mJy. Six sources were found to have extended structure in the 4.8 GHz data. The fluxes of these sources are determined using CLEAN over a larger region which is customized to roughly fit the profile of the source. However, because of the difficulty in extracting the full extended structure, the fluxes of these sources are still considered uncertain. These sources are identified via footnote in Table 1 and are not used in the characterization of the 4.8 to 28.5 GHz spectral index distribution.

We compute spectral indices between 1.4 and 28.5 GHz for point sources in cluster fields (selected at 28.5 GHz) where index α is defined by $S \propto \nu^{-\alpha}$. If we use only the 87 sources with detections in NVSS, FIRST, or the VLA maps and omit the 4 sources lacking 1.4 GHz detections, the resulting mean spectral index is $\alpha = 0.70$ with an rms dispersion of 0.34. If we include limits for the 4 sources lacking 1.4 GHz detections, the mean spectral index $\alpha = 0.66$ with an rms dispersion of 0.38, indicating that the bias due to omitting these four sources is small. We use the 87 sources with NVSS, FIRST, or VLA counterparts for the remainder of our spectral index analysis. A histogram of spectral indices for these 87 sources is shown in Figure 1. Characterizations of the spectral index distribution are given in Table 3. The distribution has a tail at low-α and is not well fit by a Gaussian. We therefore also

[8]The VLA is operated by the National Radio Astronomy Observatory, a facility of the National Science Foundation, operated under cooperative agreement by Associated Universities, Inc.

compute the median of the distribution, as well as the 25th and 75th percentiles and find them to be 0.76, 0.55, and 0.95, respectively. The mean spectral index between 4.8 and 28.5 GHz for the 19 non-extended sources in the 24 cluster subsample is $\alpha = 0.64$, with an rms dispersion of 0.39. The median of the distribution is 0.64, with 25% and 75% levels at 0.35 and 0.90.

While the beam attenuation factor is potentially a significant source of uncertainty for sources at large radius, we find that excluding sources at large radius (attenuation factor greater than 5) did not change the results. We choose a maximum cutoff outer radius of 6.6 arcmin for BIMA and 4.2 arcmin for OVRO, corresponding to a beam attenuation factor of about 30 and spanning a region twice the FWHM of the primary beam. When a source has observations from both BIMA and OVRO, we choose the one with the best combination of sensitivity and survey area.

The radial distribution of spectral indices is shown in Figure 2; there is no apparent trend in spectral index with radius from the cluster center. We compare the spectral index distribution of the central regions of cluster fields ($r < 0.5$ arcmin) with the distribution of the outer regions of cluster fields ($r > 0.5$ arcmin) and find that they are consistent with each other. The mean spectral index for the central regions of cluster fields is $\alpha = 0.77$ with an rms dispersion of 0.27 and the mean spectral index for the outer regions of cluster fields is $\alpha = 0.68$ with an rms dispersion of 0.36. The medians are 0.77 [0.56 (25%), 0.97 (75%)] for the central regions and 0.74 [0.52 (25%), 0.92 (75%)] for the outer regions. The results of a Kolmogorov-Smirnov (KS) test indicate that the distribution of spectral indices of sources in the inner regions of cluster fields is consistent with that of the outer regions. The maximum distance between their cumulative distribution functions is 0.14, corresponding to an 89% probability that the two samples are drawn from the same distribution. Since we have few sources in non-cluster fields, we do not compute an average spectral index for this group.

We compare the spectral index distribution of our mJy cluster sources to those of somewhat brighter field sources measured by the CBI (Mason et al. 2003) and Ryle groups (Waldram et al. 2003; Bolton et al. 2004). A summary is given in Table 3. Mason et al. (2003) find a spectral index from 1.4 to 31 GHz of 0.45 with an rms dispersion of 0.37. In the 9C survey, Waldram et al. (2003) compute spectral indices from 1.4 to 15.2 GHz using 465 sources at a limiting flux of 25 mJy and 84 sources with flux greater than 100 mJy. As a follow-up to the 9C survey, Bolton et al. (2004) compute indices between several frequencies from 1.4 to 43 GHz, also with a fainter sample and a brighter sample. For the fainter sample, the mean spectral index is ~ 0.4 for the lower frequencies, and steepens to ~ 0.9 from 15.2 to 43 GHz. Our spectral indices are somewhat steeper than the spectral indices measured by CBI and much steeper than those of the $\sim$ Jy point sources ($\alpha \sim 0$) measured by WMAP (Bennett

et al. 2003). Waldram et al. (2003) and Bolton et al. (2004) also find a greater percentage of sources with a flat or rising spectrum in samples of brighter sources. When comparing point source surveys, it is essential to consider the flux and frequency at which the sources are selected. We expect a survey of bright sources selected at high frequency to have a flatter spectral index than a survey of low flux sources selected at lower frequency. Our results are for a relatively low flux survey selected at high frequency, and it is interesting that the spectral index is relatively steep. The sources in our survey primarily lie in the environments of rich galaxy clusters and it is possible that there are significant differences between this population of sources and that which is found by surveys not targeting clusters.

As we look at sources with higher redshift, the emission frequency of the radiation increases. We might, therefore, expect these sources to have steeper spectral indices. However, we are now selecting sources at higher frequency which might bias the sample toward flatter spectral indices. In Figure 3, we plot spectral index as a function of cluster redshift and see no clear trend. The mean and rms dispersion in the spectral index are 0.70 and 0.35 for $z < 0.5$, 0.71 and 0.29 for $z > 0.5$, and 0.77 and 0.19 for $z > 0.8$.

5. SOURCE COUNTS

5.1. Analysis

With the field selection effects in mind from Section 2.2, we compute the differential source counts as a function of flux, dN/dS, in several flux bins, accounting for the varying noise levels from field to field. We chose the flux bins in order to maximize the number of sources used and to have a similar number of sources in each bin.

The survey boundary of each field for a given flux bin is set by the noise level of the field. For each flux bin and field, the minimum level in the flux bin sets the allowable beam-corrected noise level and the corresponding maximum attenuation radius for the field. For example, for $\geq 5\sigma$ sources in a flux bin of 1.5 - 2.5 mJy, the allowable beam-corrected noise level is $1.5/5 = 0.3$ mJy. This noise level sets the attenuation radius for the field, the radius at which the beam attenuation factor = (beam corrected noise level)/(uncorrected noise level). We set an outer boundary on the survey area for the field using the lesser of the attenuation radius or a maximum cutoff outer radius away from the field pointing center. We choose a maximum cutoff outer radius of 6.6 arcmin for BIMA and 4.2 arcmin for OVRO, corresponding to a beam attenuation factor of about 30 and spanning a region twice the FWHM of the primary beam. We treat this as a hard maximum cutoff; even if the noise is sufficiently low to allow us to go to greater radii in our sampling of a field, we do not. The

outer boundary is measured relative to the field pointing center.

We further break the data into radial bins from the cluster center. The cluster center is determined by the location of the SZE decrement. For fields without a SZE decrement detection, the pointing center is used as the center of the field. For each field, flux bin, and radial bin, we compute the survey area within the boundary set by the radial bin and the noise level for the field. Typically the survey region for a given field, flux bin, and radial bin is a circle or annulus, sometimes cut off by the noise boundary. We compute the total survey area for each flux bin by adding up the area in all the fields. When a field has observations from both BIMA and OVRO, we choose the one with the best combination of sensitivity and survey area.

For each field we identify all $\geq 5\sigma$ sources in the survey area that fall between the minimum and maximum fluxes of each flux bin. We count up the sources in each flux bin to get raw total source counts in the total survey area. The errors for the raw counts in each bin are assumed to be Poisson distributed. Differential source counts (dN/dS) and the associated errors are calculated by dividing the total raw counts in each bin by the total survey area for the corresponding flux bin and by the flux bin width.

5.2. Results and Discussion

Differential source counts (dN/dS), the number of sources, and the survey area for each flux bin are given in Figure 4 and Table 4 for the central regions of the cluster fields (radii ≤ 0.5 arcmin), the outer regions of the cluster fields (radii ≥ 0.5 arcmin), and for the non-cluster fields. The error bars on dN/dS are the Poisson errors on the raw source counts and do not include other sources of uncertainty. Typical raw counts of sources are ~ 4 in each flux bin for the inner regions of the cluster fields and ~ 8 for the outer cluster regions. We only detect two $\geq 5\sigma$ sources in the 8 non-cluster fields that were selected without regard to possible point source contamination.

The differential source counts can be described by a power law, $d\mathrm{N(S)}/d\mathrm{S} = N_0(S/S_0)^{-\gamma}$, where $S_0 = 1\,\mathrm{mJy}$ for this analysis. Best fits using a Markov chain algorithm to simultaneously estimate the normalizations for the inner, outer, non-cluster regions, and a common power law index are shown with the data in Figure 4 and are given in Table 5. The best fit common power law index is $\gamma = -1.98^{+0.20}_{-0.21}$. Best fit power-laws for the central and outer cluster regions individually are also shown in Figure 4 and Table 5. All uncertainties represent 68% confidence intervals unless otherwise noted. Source counts are found to be greatly elevated toward the central core of the cluster fields. Using the normalizations from the best

simultaneous fit, counts are found to be a factor of $8.9^{+4.3}_{-2.8}$ higher in the central regions than in the outer regions of the cluster fields. Counts are also elevated in the outer regions of the cluster fields relative to the non-cluster fields by a factor of $3.3^{+4.1}_{-1.8}$. As a cross-check, we compute dN/dS for the BIMA and OVRO fields separately and find good agreement; see Figure 5.

It is possible that gravitational lensing of background radio galaxies could lead to an enhancement of detected sources in the direction of massive galaxy clusters. A gravitational lens with magnification factor μ will modify the source counts to $d\mathrm{N}'(\mathrm{S})/d\mathrm{S} = (d\mathrm{N}'(\mathrm{S}/\mu)/d\mathrm{S})/\mu^2$. If the unlensed source counts can be described by a power law, $d\mathrm{N}(\mathrm{S})/d\mathrm{S} \propto S^{-\gamma}$, then the source counts will be changed by a factor $B = (d\mathrm{N}'(\mathrm{S})/d\mathrm{S})/(d\mathrm{N}(\mathrm{S})/d\mathrm{S}) = \mu^{-2+\gamma}$ (Blain 2002). The mean magnification in the BIMA and OVRO cluster fields is estimated by Cooray et al. (1998) to be $\mu \sim 1.4$. In this analysis, we temporarily assume that all sources are background sources drawn from the same distribution and capable of being lensed. Using the best joint fit power law index of $\gamma = 1.98^{+0.20}_{-0.21}$ we expect a factor of $B = 0.99^{+0.07}_{-0.06}$ *fewer* sources in the direction of the clusters. Therefore we conclude that, regardless of the magnification, gravitational lensing can not be responsible for the significant excess of sources seen in the direction of clusters.

In Figure 6, we compare our measurements of dN/dS with the Toffolatti et al. (1998) 30 GHz model and with measurements from other experiments, including WMAP, DASI, VSA, and CBI, which all examine non-cluster fields. We present source counts in terms of $log_{10}(S^{5/2}dN/dS)$, for ease of comparison. Counts in our non-cluster fields are consistent with those expected from the model and from extrapolations from other experiments, though with only two $\geq 5\sigma$ point sources in those fields, the sample variance is large. The source counts toward cluster fields have a similar power law slope, but have a higher normalization than expected from extrapolations of measurements of sky not concentrated on clusters.

5.3. Redshift Dependence

The overabundance of point sources toward cluster fields (especially in the central regions) implies that the sources are associated with the clusters. Therefore, we can use the redshift for each cluster to calculate the luminosities of point sources in the cluster fields and compute counts as a function of luminosity. The data have been k-corrected using a spectral index of 0.7, i.e., the luminosity at 28.5 GHz, $L_{28.5} = L(1+z)^{0.7}$. We assume a flat cosmology with $\Omega_\Lambda = 0.7$ and $H_0 = 70$ km/s/Mpc to convert observed angle to a physical distance from the cluster center. At low redshift, the clusters subtend large angles. In order for the counts to be unbiased by the angular limit set by the attenuation of the primary beam (see

Section 5.1), we impose a physical radius cut-off that corresponds to an angle over which we have good sensitivity for all redshifts. We include only sources that fall within 0.5 Mpc of the cluster center, and divide the data into three redshift bins: $0.0 < z < 0.2$, $0.2 < z < 0.4$, and $0.4 < z < 1.0$. From Figure 7, which shows source counts as a function of luminosity at 28.5 GHz, there is no clear evidence for evolution with redshift.

According to models derived from a flux limited ($S > 100$ mJy at 2.7 GHz) sample of 168 radio sources, the radio luminosity function undergoes positive evolution in the field at redshifts $z < 2$, with a reversal at higher redshifts (Dunlop & Peacock 1990). In addition, morphology studies of galaxies in massive clusters demonstrate an evolution from an early type population representing only $\approx 40\%$ of the total cluster galaxies at $z = 1$ to $\approx 80\%$ at $z = 0$ (van Dokkum & Franx 2001). Considering the observed evolution of field radio sources and of galaxies in the cluster environment, the result from the BIMA/OVRO sample of clusters initially comes as a surprise. However, this result agrees with and extends the results of Massardi & De Zotti (2004), who see no evidence for redshift evolution at $z < 0.4$ using a cross-correlation of the 1.4 GHz FIRST catalog with the Abell cluster catalog. Perlman et al. (2004) also report no evidence for strong evolution in cluster radio galaxies out to $z \sim 0.65$ from a deep radio survey of 17 clusters.

We consider two possible explanations for the discrepancy described above. First, the BIMA/OVRO sample consists of massive, X-ray selected galaxy clusters. Although at different redshifts, these massive clusters may be similar in age and provide comparable environments for the AGNs fueling radio sources. Future SZE observations should demonstrate whether evolution of the radio luminosity function at smaller cluster masses more closely resembles evolution in the field. Another possible explanation for the apparent discrepancy follows the argument presented by Waddington et al. (1998). In a much deeper flux limited ($S > 1$ mJy at 1.4 GHz) sample of radio sources, they find that the radio luminosity function does not evolve as quickly at low luminosities as that observed by Dunlop & Peacock (1990). It is likely that the difference can be explained by two different populations of point sources. The brighter sources may be dominated by a positively evolving population of quasars or powerful edge-brightened Fanaroff & Riley (1974) (FR) type II sources, while the fainter sources which are found in the BIMA/OVRO clusters may be a longer lived, lower power population of FR I sources.

6. CONCLUSIONS

From deep interferometric observations of radio point sources toward 90 fields centered on massive galaxy clusters and 8 non-cluster fields, we find that differential source counts

are greatly elevated in the centers of cluster fields. Counts are a factor of $8.9^{+4.3}_{-2.8}$ higher in central regions (radii $\leq$ 0.5 arcmin) than in the outer regions (radii $\geq$ 0.5 arcmin) of the cluster fields. Counts in our non-cluster fields are consistent with those expected from models and from extrapolations from other experiments. Additionally, source counts in the outer regions of cluster fields are a factor of $3.3^{+4.1}_{-1.8}$ higher than counts in non-cluster fields. We see no evidence for evolution of the radio source luminosity function in massive galaxy clusters out to a redshift of 1.0.

Using the NVSS and other surveys, we find a mean spectral index for sources in cluster fields between 1.4 and 28.5 GHz of $\alpha = 0.70$ with rms dispersion of 0.34, where flux $S \propto \nu^{-\alpha}$. The distribution is skewed, with a median spectral index of 0.76 [0.55 (25%), 0.95 (75%)]. This is steeper than spectral indices of brighter ($\sim$ 20 mJy) field point sources, and much steeper than those of much brighter ($\sim$ Jy) field point sources measured by other surveys. Spectral indices of sources in the outer regions of the clusters fields are consistent with those in the inner regions.

These results can be used for improving forecasts for radio source contamination of SZE and CMB experiments. The cluster fields used in this work were chosen to contain massive clusters and the sources were identified at 28.5 GHz. We anticipate that the SZA and other instruments will be able to extend this work to less massive clusters and to sources identified at yet higher frequencies.

We gratefully acknowledge the excellent support of the BIMA and OVRO staff over the many years of the OVRO/BIMA SZE program, including J.R. Forster, C. Giovanine, R. Lawrence, S. Padin, R. Plambeck, S. Scott and D. Woody. We thank C. Alexander, A. Cooray, L. Grego, G. Holder, A. Miller, J. Mohr, S. Patel and P. Whitehouse for their contributions to the SZE instrumentation, observations, and analysis.

This work was supported in part by NASA LTSA grant NAG5-7985, NSF grants PHY-0114422 and AST-0096913, the David and Lucile Packard Foundation, the McDonnell Foundation, and a MSFC director's discretionary award. Research at the Owens Valley Radio Observatory and the Berkeley-Illinois-Maryland Array was supported by NSF grants AST 99-81546 and 02-28963. For much of this work, KC was supported by NSF grant AST-0104465 under the Astronomy and Astrophysics Postdoctoral Fellowship program at the University of Chicago Department of Astronomy and Astrophysics and the Adler Planetarium and Astronomy Museum. SL acknowledges support from the NASA Graduate Student Researchers Program.

REFERENCES

Allen, S. W. et al. 1992, MNRAS, 259, 67

Bennett, C. L. et al. 2003, ApJS, 148, 97

Blain, A. W. 2002, MNRAS, 330, 219

Böhringer, H. et al. 2000, ApJS, 129, 435

Bolton, R. C. et al. 2004, MNRAS, 354, 485

Carlstrom, J. E., Joy, M., & Grego, L. 1996, ApJ, 456, L75

Cavaliere, A., & Fusco-Femiano, R. 1976, A&A, 49, 137

—. 1978, A&A, 70, 677

Cleary, K. A. et al. 2005, MNRAS, 360, 340

Condon, J. J., Cotton, W. D., Greisen, E. W., Yin, Q. F., Perley, R. A., Taylor, G. B., & Broderick, J. J. 1998, AJ, 115, 1693

Cooray, A. R., Grego, L., Holzapfel, W. L., Joy, M., & Carlstrom, J. E. 1998, AJ, 115, 1388

Crawford, C. S., Allen, S. W., Ebeling, H., Edge, A. C., & Fabian, A. C. 1999, MNRAS, 306, 857

Crawford, C. S., Edge, A. C., Fabian, A. C., Allen, S. W., Bohringer, H., Ebeling, H., McMahon, R. G., & Voges, W. 1995, MNRAS, 274, 75

Dahle, H., Kaiser, N., Irgens, R. J., Lilje, P. B., & Maddox, S. J. 2002, ApJS, 139, 313

Dawson, K. S., Holzapfel, W. L., Carlstrom, J. E., Joy, M., & LaRoque, S. J. 2006, ApJ, in press

Dawson, K. S., Holzapfel, W. L., Carlstrom, J. E., Joy, M., LaRoque, S. J., Miller, A. D., & Nagai, D. 2002, ApJ, 581, 86

Donahue, M., Voit, G. M., Scharf, C. A., Gioia, I. M., Mullis, C. R., Hughes, J. P., & Stocke, J. T. 1999, ApJ, 527, 525

Dressler, A., Smail, I., Poggianti, B. M., Butcher, H., Couch, W. J., Ellis, R. S., & Oemler, A. J. 1999, ApJS, 122, 51

Dunlop, J. S., & Peacock, J. A. 1990, MNRAS, 247, 19

Ebeling, H., Edge, A. C., Allen, S. W., Crawford, C. S., Fabian, A. C., & Huchra, J. P. 2000a, MNRAS, 318, 333

Ebeling, H., Edge, A. C., Bohringer, H., Allen, S. W., Crawford, C. S., Fabian, A. C., Voges, W., & Huchra, J. P. 1998, MNRAS, 301, 881

Ebeling, H., Edge, A. C., Fabian, A. C., Allen, S. W., Crawford, C. S., & Boehringer, H. 1997, ApJ, 479, L101

Ebeling, H., Edge, A. C., & Henry, J. P. 2001a, ApJ, 553, 668

Ebeling, H., Jones, L. R., Fairley, B. W., Perlman, E., Scharf, C., & Horner, D. 2001b, ApJ, 548, L23

Ebeling, H. et al. 2000b, ApJ, 534, 133

Ebeling, H., Voges, W., Bohringer, H., Edge, A. C., Huchra, J. P., & Briel, U. G. 1996a, MNRAS, 283, 1103

—. 1996b, MNRAS, 281, 799

Edge, A. C., Ebeling, H., Bremer, M., Röttgering, H., van Haarlem, M. P., Rengelink, R., & Courtney, N. J. D. 2003, MNRAS, 339, 913

Fairley, B. W., Jones, L. R., Scharf, C., Ebeling, H., Perlman, E., Horner, D., Wegner, G., & Malkan, M. 2000, MNRAS, 315, 669

Fanaroff, B. L., & Riley, J. 1974, MNRAS, 167, 31

Gioia, I. M., & Luppino, G. A. 1994, ApJS, 94, 583

Gioia, I. M., Maccacaro, T., Schild, R. E., Wolter, A., Stocke, J. T., Morris, S. L., & Henry, J. P. 1990, ApJS, 72, 567

Gladders, M. D., Hoekstra, H., Yee, H. K. C., Hall, P. B., & Barrientos, L. F. 2003, ApJ, 593, 48

Gladders, M. D., & Yee, H. K. C. 2005, ApJS, 157, 1

Grego, L., Carlstrom, J. E., Reese, E. D., Holder, G. P., Holzapfel, W. L., Joy, M. K., Mohr, J. J., & Patel, S. 2001, ApJ, 552, 2

Henry, J. P. et al. 1997, AJ, 114, 1293

Holder, G. P. 2002, ApJ, 580, 36

Hughes, J. P., & Birkinshaw, M. 1998, ApJ, 501, 1

Jones, L. R., Scharf, C., Ebeling, H., Perlman, E., Wegner, G., Malkan, M., & Horner, D. 1998, ApJ, 495, 100

Knox, L., Holder, G. P., & Church, S. E. 2004, ApJ, 612, 96

Kovac, J. M., Leitch, E. M., Pryke, C., Carlstrom, J. E., Halverson, N. W., & Holzapfel, W. L. 2002, Nature, 420, 772

LaRoque, S. J. et al. 2003, ApJ, 583, 559

LaRoque, S. J., Reese, E. D., Carlstrom, J. E., Holder, G., Holzapfel, W. L., Joy, M., & Grego, L. 2002, astro-ph/0204134

LaRoque, S. L., Bonamente, M., Carlstrom, J., Joy, M. K., Nagai, D., Reese, E. D., & Dawson, K. S. 2006, ApJ, submitted

Luppino, G. A., & Gioia, I. M. 1995, ApJ, 445, L77

Maccacaro, T., Wolter, A., McLean, B., Gioia, I. M., Stocke, J. T., della Ceca, R., Burg, R., & Faccini, R. 1994, Astrophys. Lett., 29, 267

Mason, B. S. et al. 2003, ApJ, 591, 540

Massardi, M., & De Zotti, G. 2004, A&A, 424, 409

Partridge, R. B., Hilldrup, K. C., & Ratner, M. I. 1986, ApJ, 308, 46

Patel, S. K. et al. 2000, ApJ, 541, 37

Perlman, E. S., Frye, C., Ebeling, H., Jones, L. R., Scharf, C. A., & Horner, D. 2004, in Clusters of Galaxies: Probes of Cosmological Structure and Galaxy Evolution, ed. J. S. Mulchaey, A. Dressler, & A. Oemler

Pospieszalski, M. W., Lakatosh, W. J., Nguyen, L. D., Lui, M., Liu, T., Le, M., Thompson, M. A., & Delaney, M. J. 1995, IEEE MTT-S Int. Microwave Symp., 1121

Reese, E. D., Carlstrom, J. E., Joy, M., Mohr, J. J., Grego, L., & Holzapfel, W. L. 2002, ApJ, 581, 53

Reese, E. D. et al. 2000, ApJ, 533, 38

Romer, A. K. et al. 2000, ApJS, 126, 209

Rudy, D. J. 1987, PhD thesis, California Institute of Technology

Scharf, C. A., Jones, L. R., Ebeling, H., Perlman, E., Malkan, M., & Wegner, G. 1997, ApJ, 477, 79

Schindler, S. et al. 1995, A&A, 299, L9

Sokasian, A., Gawiser, E., & Smoot, G. F. 2001, ApJ, 562, 88

Stocke, J. T., Morris, S. L., Gioia, I. M., Maccacaro, T., Schild, R., Wolter, A., Fleming, T. A., & Henry, J. P. 1991, ApJS, 76, 813

Struble, M. F., & Rood, H. J. 1999, ApJS, 125, 35

Sunyaev, R. A., & Zel'dovich, Y. B. 1970, Comments Astrophys. Space Phys., 2, 66

—. 1972, Comments Astrophys. Space Phys., 4, 173

Tegmark, M., Eisenstein, D. J., Hu, W., & de Oliveira-Costa, A. 2000, ApJ, 530, 133

Toffolatti, L., Argueso Gomez, F., de Zotti, G., Mazzei, P., Franceschini, A., Danese, L., & Burigana, C. 1998, MNRAS, 297, 117

Toffolatti, L., De Zotti, G., Argüeso, F., & Burigana, C. 1999, in ASP Conf. Ser. 181: Microwave Foregrounds, ed. A. de Oliveira-Costa & M. Tegmark, 153–+

van Dokkum, P. G., & Franx, M. 2001, ApJ, 553, 90

Waddington, I., Dunlop, J. S., Peacock, J. A., & Windhorst, R. A. 1998, ApJ, 500, L111

Waldram, E. M., Pooley, G. G., Grainge, K. J. B., Jones, M. E., Saunders, R. D. E., Scott, P. F., & Taylor, A. C. 2003, MNRAS, 342, 915

White, R. L., Becker, R. H., Helfand, D. J., & Gregg, M. D. 1997, ApJ, 475, 479

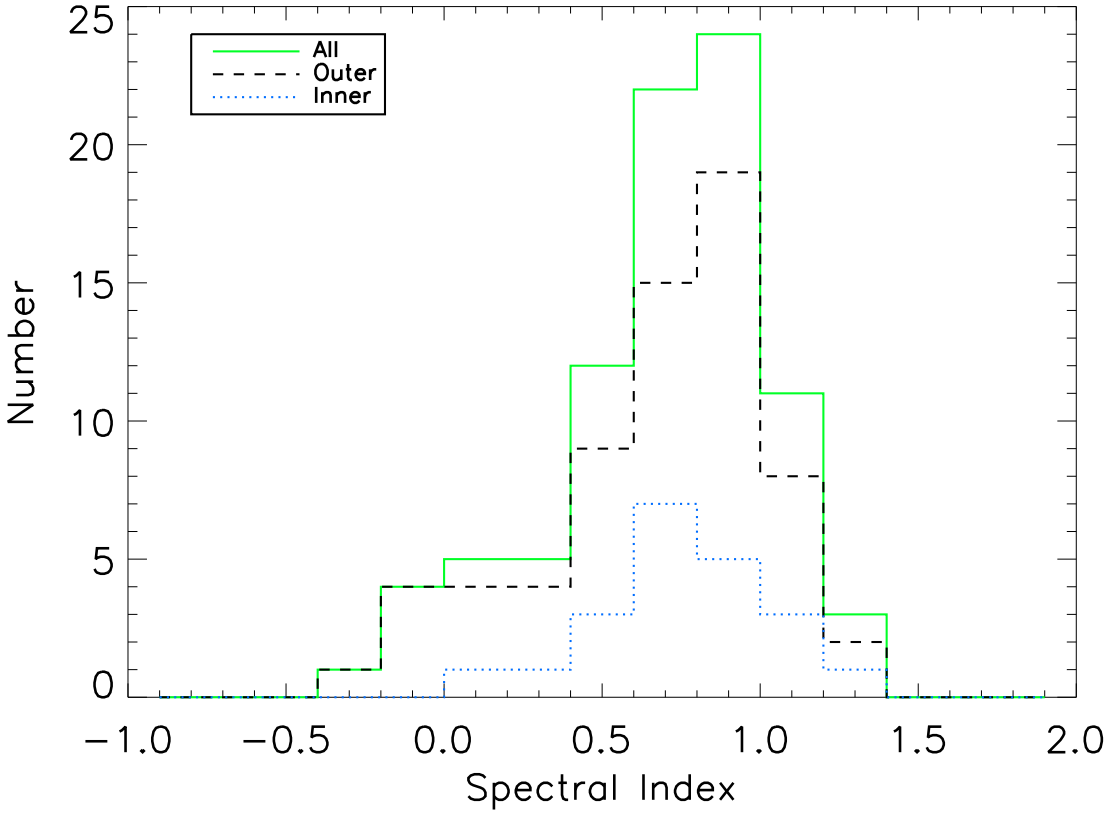

Fig. 1.—: Histogram of the spectral index distribution for point sources in cluster fields. The spectral index α is defined by $S \sim \nu^{-\alpha}$. The distribution for 87 sources is shown with a solid (green) line, the distribution for the 66 sources in the outer regions of cluster fields ($r > 0.5$ arcmin) is shown with a dashed (black) line, and the distribution for the 21 sources in the inner regions of cluster fields ($r < 0.5$ arcmin) is shown with a dotted (blue) line. The overall mean spectral index is $\alpha = 0.70$ with an rms dispersion of 0.34. The mean spectral index for the outer regions of cluster fields is $\alpha = 0.68$ with an rms dispersion of 0.36 and the mean spectral index for the the inner regions of cluster fields is $\alpha = 0.77$ with an rms dispersion of 0.27. The medians are 0.76, 0.74, and 0.77 for all, outer, and inner, respectively.

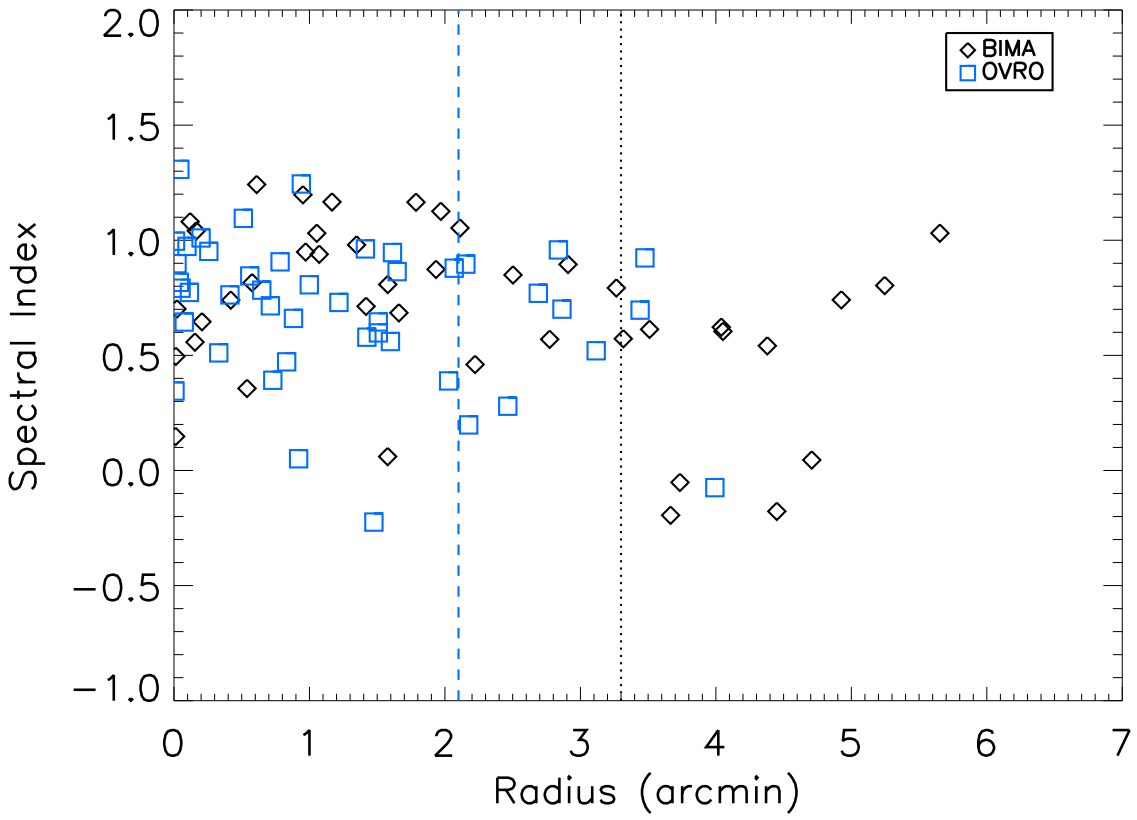

Fig. 2.—: Spectral index as a function of radius for 87 cluster sources. The figure shows no clear trend with radius. The half power point for BIMA is shown as a dotted (black) line and the half power point for OVRO is shown as a dashed (blue) line. Beyond the half power point, the beam attenuation factor becomes a potentially important source of systematic uncertainty. When a source has observations from both BIMA and OVRO, we choose the field with the best combination of sensitivity and survey area; repeat sources are not shown here.

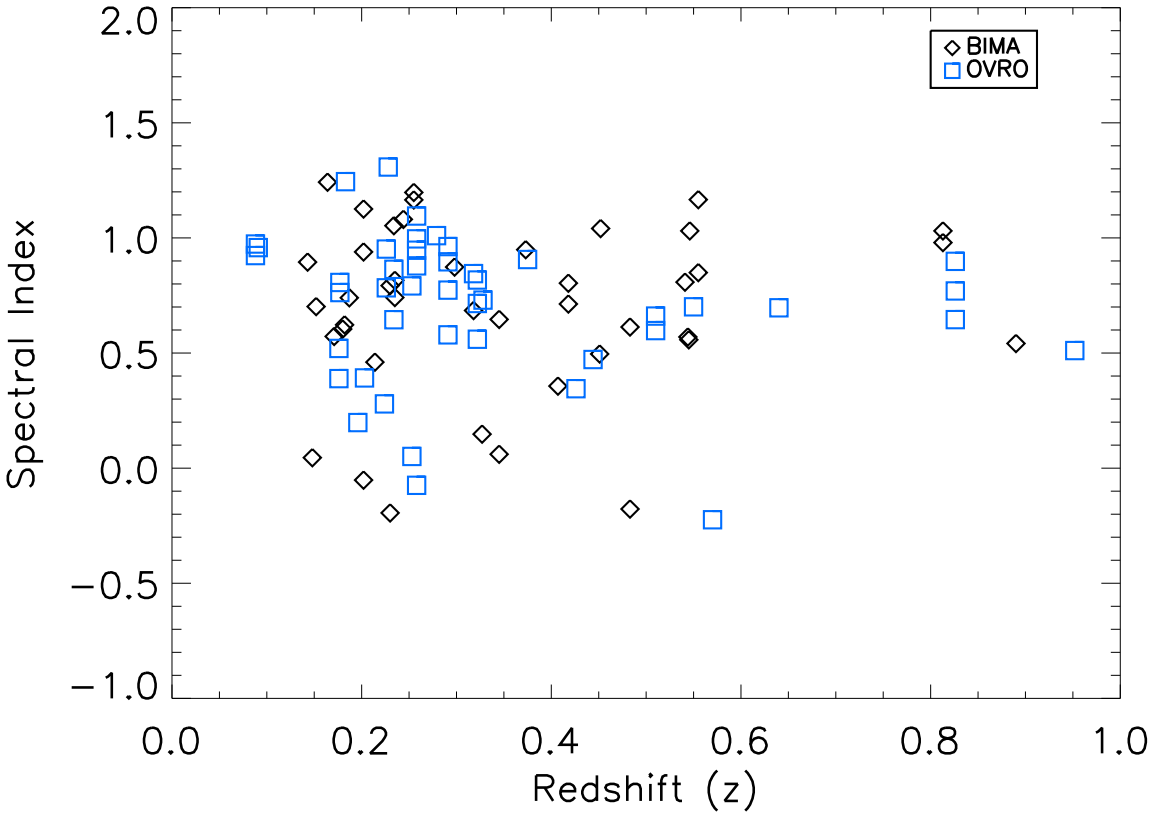

Fig. 3.—: Spectral index as a function of redshift for 87 cluster sources. The figure shows no clear trend with redshift. When a source has observations from both BIMA and OVRO, we choose the field with the best combination of sensitivity and survey area; repeat sources are not shown here.

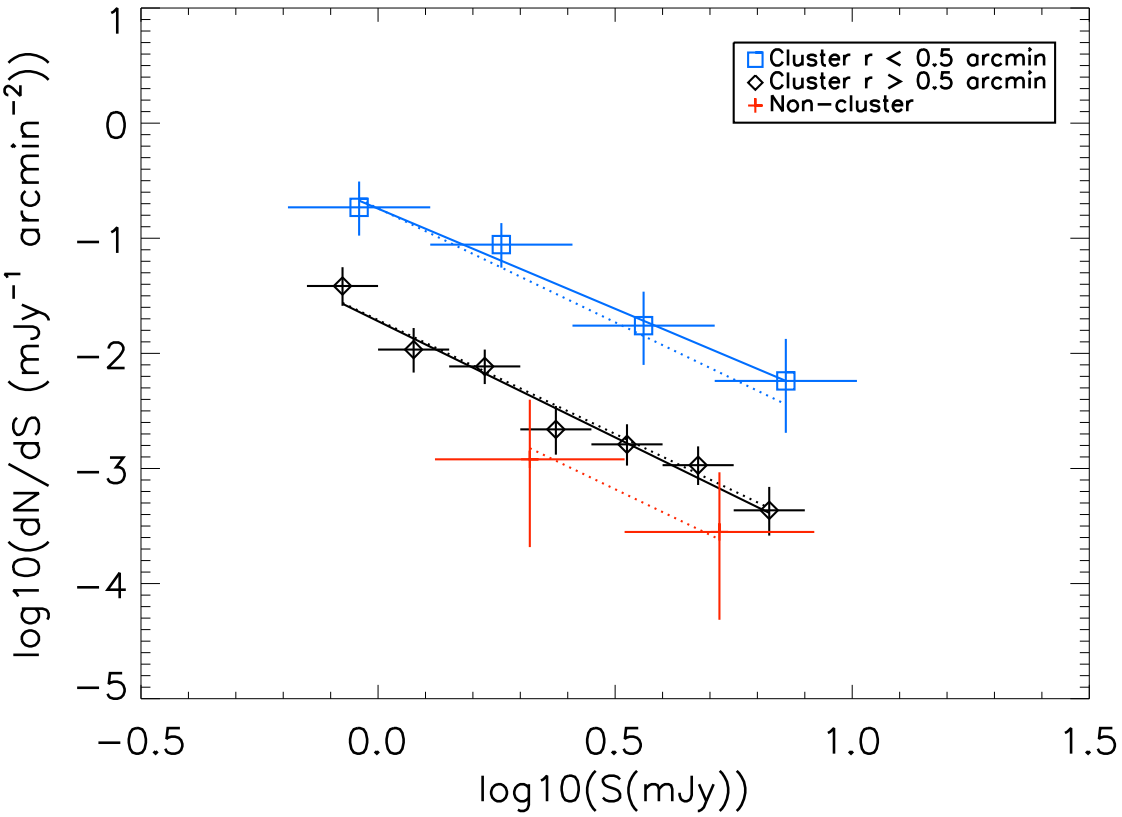

Fig. 4.—: Differential number counts, $log_{10}(dN/dS)$, as a function of flux, $log_{10}(S)$, and best fit power laws for the central regions of cluster fields ($r < 0.5$ arcmin), outer regions of cluster fields ($r > 0.5$ arcmin), and non-cluster fields. Solid lines are the best fit power laws for each set individually and dotted lines are the best fits using a Markov chain algorithm to simultaneously estimate the normalizations and a common power law index. Using the best joint fit normalizations, we find that counts in the outer regions of clusters are a factor of $3.3^{+4.1}_{-1.8}$ higher than counts in the field. Counts in the inner regions of clusters are a factor of $8.9^{+4.3}_{-2.8}$ higher than the outer regions. The outer boundary used for the outer regions of cluster fields is set by the noise levels in the fields as described in Section 5.1. Error bars on the data come from Poisson errors on raw counts and do not include other sources of uncertainty.

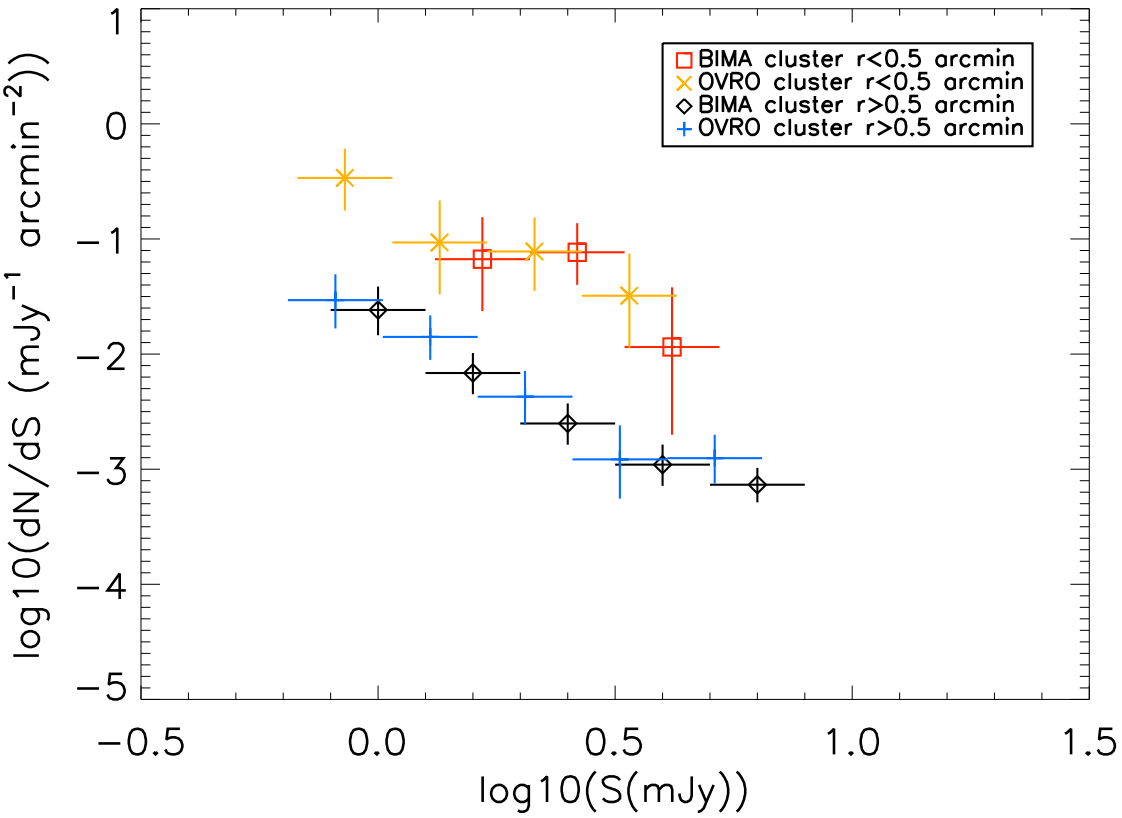

Fig. 5.—: Differential number counts as a function of flux for cluster fields taken at BIMA and OVRO respectively. They are in good agreement.

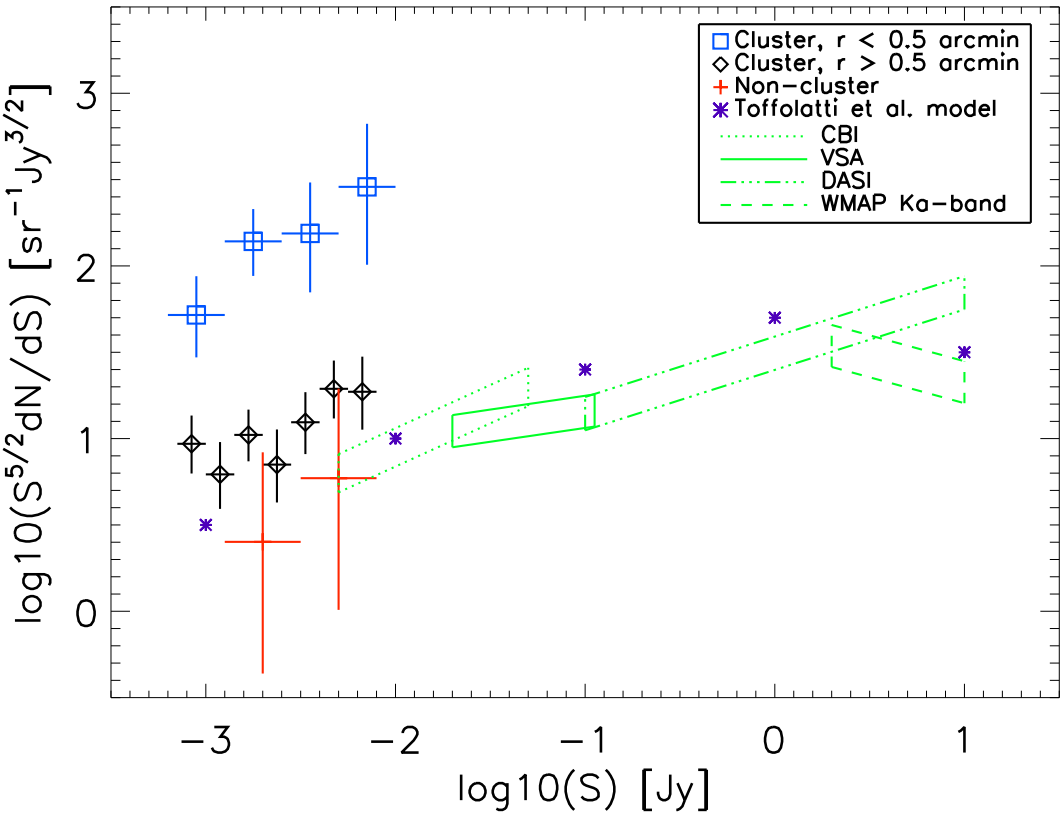

Fig. 6.—: Differential number counts as a function of flux. Point sources are overdense in cluster fields, especially within the central 0.5 arcmin. Our SZE data are shown along with measurements from CBI (Mason et al. 2003), VSA (Cleary et al. 2005), DASI (Kovac et al. 2002), and WMAP Ka-band (Bennett et al. 2003) as well as the 30 GHz model from Toffolatti et al. (1998). Counts in non-cluster fields are consistent with the model and extrapolations from other experiments.

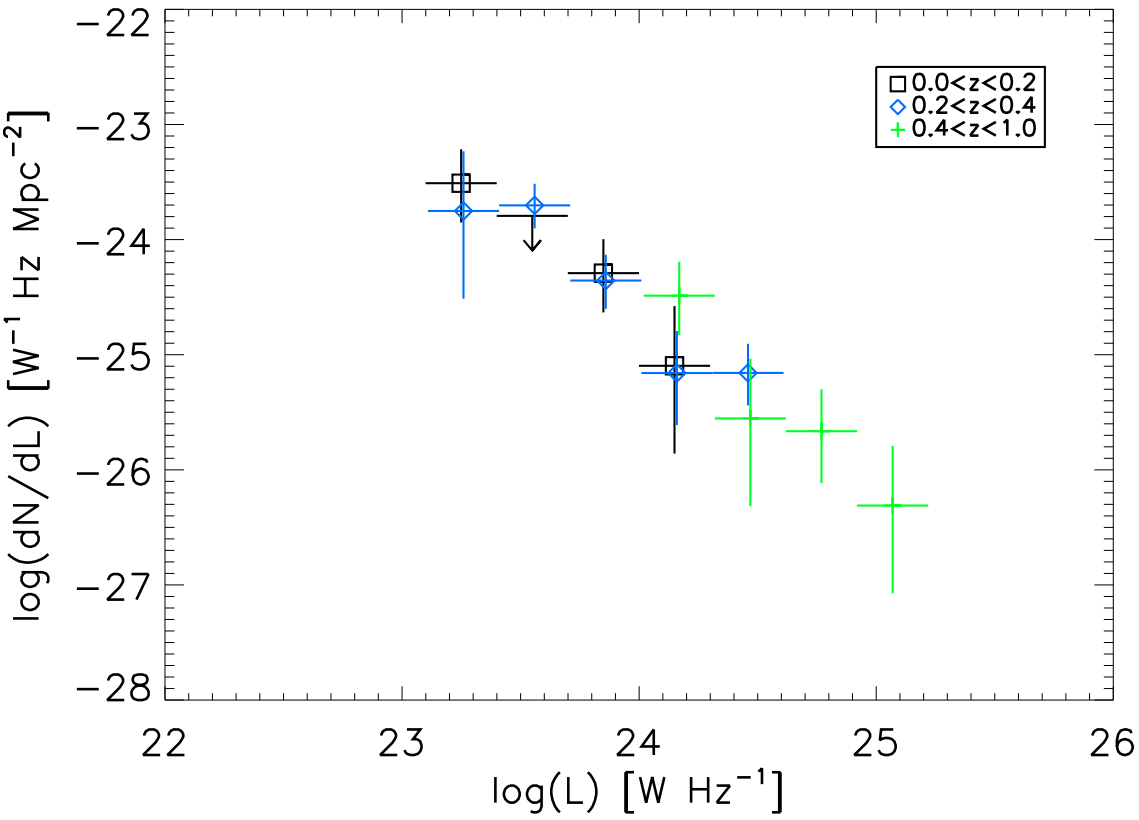

Fig. 7.—: Luminosity function, dN/dL at 28.5 GHz, in three redshift bins ($0.0 < z < 0.2$, $0.2 < z < 0.4$, $0.4 < z < 1.0$). The counts include all sources detected after imposing a cluster physical radius cutoff of 0.5 Mpc. The $z < 0.2$ plot has no counts in the second luminosity bin and we replace it with an upper limit representing the 95% confidence Poisson error. There is no clear evidence for redshift evolution in the observed luminosity function.

Table 1. Radio Point Sources in Cluster Fields

Field	z	ref	Pointing Center		Array	30GHz RMS	SZ Decrement		28.5 GHz Point Source						1.4GHz Flux	4.8GHz Flux
			α(J2000)	δ(J2000)		(mJy)	$\Delta\alpha('')$	$\Delta\delta('')$	src	$\Delta\alpha('')$	$\Delta\delta('')$	Flux (mJy)	bm atten	S/N	(mJy)	(mJy)
CL 0016+16	0.546	1	00:18:34.6	16:26:18	BIMA	0.131	−20.6	−14.2	1	−49.5	−335.6	12.1	9.3	9.9	269.3	90.6
CL J0018.8+1602	0.541	2	00:18:47.9	16:02:22	BIMA	0.180	···	···	1	−93.7	−13.5	2.3	1.2	11.1	26.6	
MACS J0025−12	0.586	3	00:22:57.8	−12:39:07	BIMA	0.312	−33.3	31.9		···	···	···	···	···	···	
					OVRO	0.229				···	···	···	···	···	···	
Cl 0024+1654	0.393	4	00:26:35.8	17:09:41	BIMA	0.085	···	···		···	···	···	···	···	···	
Abell 68	0.255	5	00:37:06.6	09:09:19	BIMA	0.097	−39.5	43.9	1	14.7	−55.2	1.6	1.1	15.6	59.1	12.6 [a]
					BIMA	0.097			2	6.6	−79.9	1.4	1.2	12.8	[b]	0.303[a]
					BIMA	0.097			3	−0.5	−107.2	1.2	1.2	10.2	40.2	8.4
MACS J0111+08	···	···	01:11:34.3	08:55:53	BIMA	0.133	···	···		···	···	···	···	···	···	
Abell 267	0.230	5	01:52:41.9	01:00:24	BIMA	0.101	5.2	1.9	1	192.0	107.2	7.5	2.3	31.8	4.2	
					OVRO	0.073			1	190.1	106.5	4.2	10.5	5.7	4.2	
					BIMA	0.101			2	−190.5	−45.6	2.8	2.0	13.9	30.0	
CL J0152.7−1357	0.83	6	01:52:43.0	−13:57:29	BIMA	0.183	−1.2	−9.2		···	···	···	···	···	···	
Abell 348	0.274	5	02:23:59.0	−08:35:39	OVRO	0.078	···	···		···	···	···	···	···	···	
RCS J0224.5−0002	0.773	7	02:24:34.0	−00:02:31	BIMA	0.112	−20.3	2.5		···	···	···	···	···	···	
					OVRO	0.094				···	···	···	···	···	···	
Abell 370	0.375	5	02:39:52.5	−01:34:20	BIMA	0.152	−1.5	−23.7	1	45.2	14.5	0.9	1.0	6.0	11.7	1.7
					OVRO	0.072			1	45.0	13.4	0.8	1.1	9.7	11.7	1.7
Abell 383	0.187	5	02:48:03.6	−03:32:10	BIMA	0.465	···	···	1	−2.6	25.0	4.4	1.0	9.4	40.9	
MS 0302.7+1658	0.426	8	03:05:31.7	17:10:03	BIMA	0.267	···	···	1	−2.5	0.9	2.7	1.0	10.1	4.8	
					OVRO	0.047	···	···	1	0.1	−0.4	1.7	1.0	36.2	4.8	
MACS J0329−02	0.467	9	03:29:40.5	−02:11:40	OVRO	0.165	···	···		···	···	···	···	···	···	
Abell 478	0.088	5	04:13:26.2	10:27:58	BIMA	0.116	−5.9	−9.1	1	−13.5	−2.8	2.3	1.0	19.4	36.9	
			04:13:25.0	10:27:59	OVRO	0.059			1	4.3	−3.8	2.0	1.0	33.3	36.9	
					BIMA	0.116			2	178.2	9.3	2.1	1.8	10.2	47.7	
					OVRO	0.059			2	208.4	7.7	3.0	7.5	6.3	47.7	
RX J0439.0+0715	0.244	10	04:39:01.2	07:15:36	BIMA	0.207	···	···	1	−0.7	−7.1	1.2	1.0	5.7	30.6	
MS 0451.6−0305	0.55	8	04:54:10.8	−03:00:57	OVRO	0.056	11.2	4.5	1	169.5	−28.2	1.8	3.6	8.5	14.9	8.16
Abell 520	0.202	5	04:54:12.7	02:55:24	BIMA	0.103	−50.0	−30.0	1	−172.7	142.8	7.8	2.4	31.2	6.7	11.4
					OVRO	0.078			1	−170.3	142.4	4.4	11.0	5.0	6.7	11.4
					BIMA	0.103			2	63.8	8.4	0.9	1.1	8.2	15.3	2.99
					OVRO	0.078			2	61.5	8.0	1.1	1.2	12.0	15.3	2.99
					BIMA	0.103			3	114.9	−27.7	0.9	1.3	7.2	27.8	9.78
					OVRO	0.078			3	116.0	−27.1	0.7	1.8	5.2	27.8	9.78
MACS J0647.7+7015	0.584	11	06:47:50.0	70:14:55	OVRO	0.061	2.9	1.1		···	···	···	···	···	···	···
MACS J0717.5+3745	0.555	12	07:17:33.8	37:45:20	BIMA	0.134	−42.3	0.0	1	40.1	−57.3	2.7	1.1	18.6	90.9	36.0 [a]
					BIMA	0.134			2	86.8	−122.5	1.5	1.5	7.8	19.8	7.1
Abell 586	0.171	5	07:32:20.3	31:38:02	BIMA	0.113	−10.3	−6.7	1	−0.3	199.0	4.4	2.0	19.6	24.8	4.02
MS 0735.6+7421	0.216	8	07:41:45.0	74:14:37	OVRO	0.219	···	···		···	···	···	···	···	···	
MACS J0744.8+3937	0.686	11	07:44:52.5	39:27:30	BIMA	0.241	−1.7	3.2		···	···	···	···	···	···	···
					OVRO	0.069				···	···	···	···	···	···	···
Abell 611	0.288	5	08:00:56.7	36:03:22	OVRO	0.038	−3.3	1.2		···	···	···	···	···	···	···
Abell 665	0.182	5	08:30:59.3	65:50:09	BIMA	0.101	−10.7	40.3	1	192.9	146.8	4.8	2.8	16.5	31.1	25.5
					OVRO	0.076				···	···	···	···	···	···	···
Abell 697	0.282	5	08:42:57.6	36:21:59	OVRO	0.041	2.6	−4.9		···	···	···	···	···	···	···
Cl 0847.2+3617	0.373	13	08:50:10.1	36:05:10	BIMA	0.160	···	···	1	34.9	−46.7	1.2	1.1	7.0	20.8	
Zw 2089	0.235	14	09:00:37.9	20:54:58	BIMA	0.223	···	···		···	···	···	···	···	···	
Abell 750	0.180	5	09:09:11.8	10:59:20	BIMA	0.160	···	···	1	−122.7	209.9	3.7	2.8	8.0	22.8	
MACS J0913+40	0.452	15	09:13:46.0	40:56:20	BIMA	0.117	2.3	6.7	1	−7.2	6.8	0.7	1.0	5.9	15.9	

Table 1—Continued

Field	z	ref	Pointing Center		Array	30GHz RMS	SZ Decrement		28.5 GHz Point Source						1.4GHz Flux	4.8GHz Flux
			α(J2000)	δ(J2000)		(mJy)	$\Delta\alpha('')$	$\Delta\delta('')$	src	$\Delta\alpha('')$	$\Delta\delta('')$	Flux (mJy)	bm atten	S/N	(mJy)	(mJy)
					OVRO	0.236				...	...	...	...	...	...	
Abell 773	0.217	5	09:17:54.5	51:43:43	BIMA	0.134	−15.0	6.3		...	...	...	...	...	...	...
					OVRO	0.078				...	...	...	...	...	...	...
Abell 781	0.298	5	09:20:28.8	30:31:08	BIMA	0.235	...	...	1	−80.2	−83.9	5.3	1.3	18.0	74.1	
Abell 851	0.407	5	09:42:56.6	46:59:20	BIMA	0.149	0.2	30.8	1	8.5	−31.2	1.1	1.1	7.0	3.1	
Zwicky 2701	0.214	16	09:52:47.5	51:53:28	BIMA	0.474	...	...	1	−40.8	−126.9	18.7	1.4	29.1	74.9	
Abell 959	0.353	5	10:17:35.9	59:34:06	OVRO	0.085	...	...		...	...	...	...	...	...	
Zwicky 3146	0.291	17	10:23:39.7	04:11:11	BIMA	0.163	5.0	6.2	1	78.9	−30.3	5.4	1.1	29.1	95.8	
					OVRO	0.074	5.0	6.2	1	79.0	−30.7	5.3	1.4	52.8	95.8	
					BIMA	0.163	5.0	6.2	2	−37.4	−126.6	2.0	1.3	9.3	31.5	
					OVRO	0.074	5.0	6.2	2	−39.6	−123.0	2.1	2.1	13.9	31.5	
					OVRO	0.074	5.0	6.2	3	−6.1	3.1	0.7	1.0	9.3	7.1	
					OVRO	0.074	5.0	6.2	4	78.7	33.3	0.6	1.2	6.3	3.6	
Abell 992	0.247	5	10:22:33.7	20:29:30	OVRO	0.060	...	...		...	...	...	...	...	...	
Abell 990	0.144	5	10:23:39.9	49:08:39	BIMA	0.852	...	...		...	...	...	...	...	...	
MS 1054.4−0321	0.826	18	10:56:59.5	−03:37:28	OVRO	0.044	−5.4	−8.2	1	0.2	1.3	0.9	1.0	21.4	14.1	
					OVRO	0.044			2	−161.3	1.7	1.8	3.0	12.8	18.2	
					OVRO	0.044			3	−24.9	−87.0	0.4	1.3	7.2	3.1	
MACS J1108+09	0.48	19	11:08:55.5	09:06:00	OVRO	0.113	10.8	8.4		...	...	...	...	...	...	
MACS J1115+53	0.51	20	11:15:14.9	53:19:56	OVRO	0.077	−3.5	13.9	1	20.7	−48.7	1.0	1.1	11.6	7.33[c]	
					OVRO	0.077			2	57.4	−70.0	0.7	1.4	6.9	4.49[c]	
Zwicky 5247	0.229	21	12:34:17.3	09:46:12	BIMA	0.379	...	...		...	...	...	...	...	...	
MS 1137+66	0.782	22	11:40:23.9	66:08:19	BIMA	0.081	−11.6	−13.9		...	...	...	...	...	...	...
Abell 1351	0.322	5	11:42:24.6	58:32:06	OVRO	0.110	...	...	1	−1.4	−1.9	6.4	1.0	57.9	74.56[c]	
					OVRO	0.110			2	−85.6	−43.2	1.9	1.5	11.5	10.03[c]	
					OVRO	0.110			3	−13.2	−40.6	0.8	1.0	7.1	7.25[c]	
MACS J1149.5+2223	0.544	11	11:49:34.3	22:23:43	BIMA	0.109	9.7	12.3	1	−165.8	−13.3	2.8	1.6	16.1	15.8	7.87 [a]
					OVRO	0.229				...	...	...	...	...	...	...
Abell 1413	0.143	5	11:55:18.0	23:24:19	BIMA	0.144	−4.2	20.6	1	−128.6	118.0	1.9	1.7	8.0	28.8	9.27 [a]
CL 1226+33	0.89	23	12:26:58.0	33:32:45	BIMA	0.116	0.6	12.9	1	259.9	−39.0	5.8	3.4	14.3	29.8	
Abell 1576	0.279	5	12:36:59.3	63:11:10	OVRO	0.108	...	...	1	−11.9	1.4	0.9	1.0	8.1	18.4	
Abell 1682	0.234	5	13:06:57.2	46:32:42	BIMA	0.422	...	...	1	−116.9	48.7	8.1	1.3	14.6	193.6	
MACS J1311.0−0311	0.519	24	13:11:01.7	−03:10:39	BIMA	0.123	8.6	−6.1		...	...	...	...	...	...	
Abell 1689	0.183	5	13:11:30.3	−01:20:25	BIMA	0.169	−17.6	−4.3	1	13.2	50.8	1.3	1.1	7.3	61.0	
					OVRO	0.059			1	18.4	53.3	1.4	1.1	21.4	61.0	
Abell 1703	0.258	5	13:15:05.3	51:49:02	OVRO	0.243	...	...	1	29.6	−8.2	1.7	1.0	6.9	47.2	
Abell 1704	0.221	5	13:14:26.0	64:34:41	OVRO	0.098	...	...		...	...	...	...	...	...	
Abell 1722	0.328	5	13:20:09.1	70:04:39	OVRO	0.124	32.0	11.5	1	27.8	67.5	0.9	1.1	6.0	8.4	
RCS J132427+2845	0.997	25	13:24:28.3	28:44:59	OVRO	0.065	...	...		...	...	...	...	...	...	
RCS J132631+2903	0.952	25	13:26:31.1	29:03:20	BIMA	0.140	−3.5	−15.1		...	...	...	...	...	...	
					OVRO	0.065			1	10.6	16.7	0.6	1.0	9.1	2.8	
Abell 1763	0.228	5	13:35:20.2	41:00:04	OVRO	0.407	...	...	1	−1.9	−1.8	16.6	1.0	40.9	857.2	
RX J1347.5−1145	0.451	26	13:47:30.7	−11:45:09	BIMA	0.188	−1.7	3.7	1	−0.6	−0.6	10.7	1.0	56.8	47.6	33.5
					OVRO	0.235			1	−1.1	0.9	9.9	1.0	42.3	47.6	33.5
MS 1358.4+6245	0.327	8	13:59:50.6	62:31:05	BIMA	0.084	−5.8	1.7	1	0.7	0.3	1.7	1.0	19.9	2.61[c]	4.39
					OVRO	0.089			1	0.3	−0.7	1.5	1.0	16.9	2.61[c]	4.39
Abell 1835	0.253	5	14:01:02.0	02:52:42	BIMA	0.137	−3.0	3.9	1	0.5	1.3	2.7	1.0	19.8	31.25[c]	
					OVRO	0.073			1	1.4	2.8	2.9	1.0	39.4	31.25[c]	
					BIMA	0.137			2	−24.2	−50.7	1.3	1.1	8.7	1.58[c]	

Table 1—Continued

Field	z	ref	Pointing Center		Array	30GHz RMS	SZ Decrement		28.5 GHz Point Source						1.4GHz Flux	4.8GHz Flux
			α(J2000)	δ(J2000)		(mJy)	$\Delta\alpha('')$	$\Delta\delta('')$	src	$\Delta\alpha('')$	$\Delta\delta('')$	Flux (mJy)	bm atten	S/N	(mJy)	(mJy)
					OVRO	0.073			2	−22.4	−50.5	1.4	1.2	16.4	1.58[c]	
RCS J1419.2+5326	0.64	7	14:19:12.1	53:26:11	OVRO	0.117	···	···	1	108.1	−175.9	15.0	7.5	16.9	122.3	
MACS J1423.8+2404	0.545	11	14:23:48.3	24:04:48	BIMA	0.121	−9.1	−10.2	1	−8.2	−4.4	1.5	1.0	12.3	8.0	4.47
Abell 1914	0.171	5	14:26:03.5	37:49:46	BIMA	0.150	−32.3	−7.9		···	···	···	···	···	···	
Abell 1995	0.318	27	14:52:57.6	58:02:56	BIMA	0.096	7.1	1.3	1	−79.8	−59.6	0.6	1.2	5.5	4.9	0.54
					OVRO	0.051			2	23.7	23.7	0.6	1.0	11.3	8.9	3.5
MS 1455.0+2232	0.258	8	14:57:15.1	22:20:34	BIMA	0.321	···	···	1	−219.3	−95.1	6.3	2.7	7.1	3.9	
					OVRO	0.037			1	−220.7	−93.2	4.9	16.3	7.1	3.9	
					OVRO	0.037			2	−0.5	0.5	1.0	1.0	26.0	19.3	
					OVRO	0.037			3	−94.8	−19.5	1.0	1.7	17.4	16.5	
					OVRO	0.037			4	−60.0	−108.7	0.9	1.8	13.1	13.2	
RXJ J1532.9+3021	0.345	14	15:32:54.2	30:21:11	BIMA	0.176	34.1	−8.0	1	−42.5	−84.6	6.6	1.2	32.2	7.9	
					BIMA	0.176			2	−4.9	−11.4	3.3	1.0	18.4	22.8	
Abell 2111	0.229	5	15:39:41.8	34:25:01	BIMA	0.091	−23.4	0.8		···	···	···	···	···	···	
Abell 2142	0.091	5	15:58:20.2	27:13:52	BIMA	0.159	17.2	19.5	1	−81.0	148.2	7.2	1.6	27.6	107.3	
					OVRO	0.063			1	−81.4	149.5	6.0	3.8	25.8	107.3	
Abell 2146	0.234	5	15:56:14.4	66:20:56	OVRO	0.148	···	···	1	−3.6	−2.8	2.2	1.0	14.8	15.3	
					OVRO	0.148			2	−61.0	77.7	3.0	1.5	13.5	40.6	
					OVRO	0.148			3	−98.6	−51.8	1.4	1.6	5.8	[d]	
Abell 2163	0.203	5	16:15:46.1	−06:08:55	BIMA	0.169	37.5	8.4	1	−36.9	12.7	1.3	1.0	7.6	4.8[e]	2.55
					OVRO	0.071			1	−41.3	14.5	1.5	1.1	19.3	4.8[e]	2.55
RCS J1620.2+2929	0.87	7	16:20:10.0	29:29:22	OVRO	0.121	···	···		···	···	···	···	···	···	
MACS J1621.3+3810	0.465	12	16:21:24.0	38:10:02	BIMA	0.127	21.6	27.7		···	···	···	···	···	···	
					OVRO	0.089				···	···	···	···	···	···	
Abell 2204	0.152	5	16:32:46.9	05:34:32	BIMA	0.122	−6.7	−11.4	1	1.1	0.8	8.4	1.0	68.5	69.3	26.0
Abell 2218	0.176	5	16:35:49.5	66:12:44	BIMA	0.124	11.8	−16.3	1	−164.4	36.0	5.2	1.6	25.6	[f]	[f]
					OVRO	0.054			1	−165.8	37.7	4.3	3.6	21.7	[f]	[f]
					BIMA	0.124			2	154.0	99.2	3.1	1.8	13.9	12.1[e]	
					OVRO	0.054			2	159.3	97.9	2.5	5.0	9.3	12.1[e]	
					BIMA	0.124			3	−11.5	120.2	1.3	1.3	8.0	4.8[e]	
					OVRO	0.054			3	−11.1	121.2	1.5	1.9	14.7	4.8[e]	
Abell 2219	0.226	5	16:40:20.7	46:42:40	OVRO	0.130	−18.7	16.5	1	13.6	7.2	13.6	1.0	103.8	239.1	
					OVRO	0.130	···	···	2	30.2	−24.5	0.7	1.0	5.4	7.9	
RXJ 1716+67	0.813	28	17:16:49.2	67:08:24	BIMA	0.112	30.1	−33.9	1	−63.2	−3.0	6.7	1.1	56.0	149.6[e]	
					BIMA	0.112			2	−79.3	15.6	5.0	1.1	39.9	95.6[e]	
					BIMA	0.112			3	16.8	30.4	0.7	1.0	6.0	[g]	
RX J1720.1+2637	0.164	10	17:20:08.9	26:38:06	BIMA	0.167	···	···	1	13.8	−33.9	2.1	1.1	12.2	87.7	
Abell 2259	0.164	5	17:20:09.7	27:40:08	BIMA	0.131	−9.9	1.0		···	···	···	···	···	···	
Abell 2261	0.224	5	17:22:27.1	32:07:59	BIMA	0.154	−2.8	1.3	1	−128.1	74.0	7.9	1.4	35.4	24.3	11.4
					OVRO	0.062			1	−127.1	75.5	10.5	2.6	65.0	34.3	11.4
Abell 2294	0.178	5	17:23:55.3	85:53:24	BIMA	0.345	···	···		···	···	···	···	···	···	
MS 2053.7−0449	0.583	8	20:56:21.8	−04:37:52	OVRO	0.031	−12.6	−4.4		···	···	···	···	···	···	
Abell 2345	0.177	5	21:27:13.6	−12:09:45	OVRO	0.194	···	···	1	−57.9	−15.5	5.1	1.2	22.6	57.6[e]	
					OVRO	0.194			1	−24.4	−4.1	3.8	1.0	19.3	38.2[e]	
MACS J2129.4−0741	0.570	11	21:29:26.0	−07:41:28	OVRO	0.072	−15.9	−4.1	2	63.0	−62.2	1.2	1.3	11.8	0.6[h]	
RX J2129.6+0005	0.235	10	21:29:37.9	00:05:38	BIMA	0.095	30.2	−26.0	1	30.3	−16.6	2.2	1.0	22.4	25.4	9.01
					BIMA	0.095			2	258.5	143.3	3.7	5.3	7.6	34.3	0.45[a]
Abell 2409	0.148	5	22:00:54.5	20:57:32	BIMA	0.106	−17.8	33.6	1	235.0	−156.8	3.4	4.3	7.4	3.9	
MACS J2214.9−1359	0.483	29	22:14:57.5	−14:00:15	BIMA	0.159	14.1	4.1	1	−263.5	−43.2	99.0	3.7	170.1	58.0	

Table 1—Continued

Field	z	ref	Pointing Center		Array	30GHz RMS (mJy)	SZ Decrement		28.5 GHz Point Source						1.4GHz Flux (mJy)	4.8GHz Flux (mJy)
			α(J2000)	δ(J2000)			$\Delta\alpha(''$)	$\Delta\delta(''$)	src	$\Delta\alpha(''$)	$\Delta\delta(''$)	Flux (mJy)	bm atten	S/N		
					OVRO	0.128			1	−261.9	−41.8	45.8	50.8	7.4	58.0	
					BIMA	0.159			2	24.4	209.2	3.8	2.2	11.0	24.2	
MACS J2228.5+2036	0.418	30	22:28:34.4	20:36:37	BIMA	0.110	−20.1	37.2	1	−25.1	−81.3	0.8	1.1	6.8	7.2	
					BIMA	0.110			2	−82.7	−303.7	4.5	6.4	6.2	50.4	
MACS J2243.3−0935	0.444	31	22:43:21.0	−09:35:25	BIMA	0.662	−35.4	12.0		···	···	···	···	···	···	
					OVRO	0.121			1	−47.0	16.6	1.4	1.1	10.5	5.8	
Abell 2507	0.196	5	22:56:51.6	05:30:12	OVRO	0.072	···	···	1	−114.2	63.3	8.1	2.1	54.4	14.8	

[a]Detected as an extended source in 4.8 GHz VLA data.

[b]No detection found in the literature. Using the 3 times the NVSS noise level, we set an upper limit on the 1.4 GHz flux of 1.35 mJy and an upper limit on the 1.4 to 28.5 GHz spectral index of 0.0.

[c]FIRST catalog.

[d]No detection found in the literature. Using the 3 times the NVSS noise level, we set an upper limit on the 1.4 GHz flux of 1.35 mJy and an upper limit on the 1.4 to 28.5 GHz spectral index of 0.0.

[e]VLA map.

[f]Using the 3 times the VLA map noise level, we set an upper limit on the 1.4 GHz flux of 0.45 mJy and an upper limit on the 1.4 to 28.5 GHz spectral index of -0.7. The source is detected at 6 cm by Partridge et al. (1986) with a flux of 2.59 mJy, which yields a spectral index of -0.4 from 5 to 28.5 GHz.

[g]No detection found in the literature. Using the 3 times the VLA map noise level, we set an upper limit on the 1.4 GHz flux of 1.32 mJy and an upper limit on the 1.4 to 28.5 GHz spectral index of +0.2.

[h]FIRST map.

Note. — References:

1. Stocke et al. (1991)
2. Hughes & Birkinshaw (1998)
3. From Chandra X-ray spectrum (observations 3521+5010, 45 ksec exposure) we obtain $z = 0.586 \pm 0.01$.
4. Dressler et al. (1999)
5. Struble & Rood (1999)
6. Romer et al. (2000)
7. Gladders et al. (2003)
8. Gioia & Luppino (1994)
9. From Chandra X-ray spectrum (observations 3257+3582+6108, 70 ksec exposure) we obtain $z = 0.467 \pm 0.005$.

10. Ebeling et al. (1998)

11. LaRoque et al. (2003)

12. Edge et al. (2003)

13. Crawford et al. (1999)

14. Dahle et al. (2002)

15. From Chandra X-ray spectrum (observation 509, 10 ksec exposure) we obtain $z = 0.452 \pm 0.005$.

16. Crawford et al. (1995)

17. Allen et al. (1992)

18. Luppino & Gioia (1995)

19. From Chandra X-ray spectrum (observations 3252+5009, 35 ksec exposure) we obtain $z = 0.48^{+0.03}_{-0.06}$.

20. From Chandra X-ray spectrum (observations 3253+5008+5350, 35 ksec exposure) we obtain $z = 0.51^{+0.04}_{-0.05}$.

21. Böhringer et al. (2000)

22. Donahue et al. (1999)

23. Ebeling et al. (2001b)

24. From Chandra X-ray spectrum (observations 3258+6110, 85 ksec exposure) we obtain $z = 0.519 \pm 0.007$.

25. Gladders & Yee (2005)

26. Schindler et al. (1995)

27. Patel et al. (2000)

28. Henry et al. (1997)

29. LaRoque et al. (2006)

30. From Chandra X-ray spectrum (observation 3285, 20 ksec exposure) we obtain $z = 0.42^{+0.01}_{-0.02}$.

31. From Chandra X-ray spectrum (observation 3260, 21 ksec exposure) we obtain $z = 0.44 \pm 0.01$.

Table 2. Radio Point Sources in Non-Cluster Fields.

Field	Pointing Center α(J2000)	Pointing Center δ(J2000)	RMS (mJy)	$\Delta\alpha(''$)	$\Delta\delta(''$)	28.5 GHz Flux (mJy)	bm atten factor	S/N	1.4 GHz Flux (mJy)	4.8 GHz Flux (mJy)
BDF4	00:28:04.4	+28:23:06	0.075	···	···	···	···	···	···	···
HDF	12:36:49.4	+62:12:58	0.080	−25.7	−87.8	0.5	1.2	5.2	···	0.59
BDF6	18:21:00.0	+59:15:00	0.068	···	···	···	···	···	···	···
BDF7	06:58:45.0	+55:17:00	0.078	···	···	···	···	···	···	···
BDF8	00:17:30.0	+29:00:00	0.089	···	···	···	···	···	···	···
BDF9	12:50:15.0	+56:52:30	0.084	···	···	···	···	···	···	···
BDF10	18:12:37.2	+58:32:00	0.086	−161.2	−169.9	1.5	2.6	6.7	···	1.67
BDF11	06:58:00.0	+54:24:00	0.090	···	···	···	···	···	···	···
BDF12	06:57:38.0	+55:32:00	0.093	···	···	···	···	···	···	···
BDF13	22:22:45.0	+36:37:00	0.088	···	···	···	···	···	···	···
BDF14	00:26:04.4	+28:23:06	0.072	···	···	···	···	···	···	···
BDF15	06:56:45.0	+55:17:00	0.076	−8.6	−321.6	7.1	7.2	12.9	4.5	9.39
BDF16	12:34:49.4	+62:12:58	0.082	···	···	···	···	···	···	···
BDF17	18:19:00.0	+59:15:00	0.083	···	···	···	···	···	···	···
BDF18	00:15:30.0	+29:00:00	0.087	···	···	···	···	···	···	···
BDF19	06:55:38.0	+55:32:00	0.084	···	···	···	···	···	···	···
BDF20	12:48:15.0	+56:52:30	0.081	247.2	16.0	1.4	3.1	5.6	4.3	3.81
BDF21	18:10:37.2	+58:32:00	0.083	···	···	···	···	···	···	···

Table 3. Spectral indices.

Data Set	Frequency Range	No. Sources	Mean Index ± RMS	Median Index [25%, 75%]	Flux Limits
Overall cluster ($r \geq 0.5$ arcmin)	1.4 to 28.5 GHz	87	0.70 ± 0.34	0.76 [0.55, 0.95]	$\sim$ 0.6 - 10.0 mJy at 28.5 GHz (see text)
Inner cluster ($r \leq 0.5$ arcmin)	1.4 to 28.5 GHz	21	0.77 ± 0.27	0.77 [0.56, 0.97]	$\sim$ 0.6 - 10.0 mJy at 28.5 GHz (see text)
Outer cluster ($r \geq 0.5$ arcmin)	1.4 to 28.5 GHz	66	0.68 ± 0.36	0.74 [0.52, 0.92]	$\sim$ 0.7 - 8.0 mJy at 28.5 GHz (see text)
4.8 GHz Subsample	4.8 to 28.5 GHz	19	0.64 ± 0.39	0.64 [0.35, 0.90]	$\sim$ 0.6 - 10.0 mJy at 28.5 GHz (see text)
Mason et al. 2003 (CBI)	1.4 to 31 GHz	56	0.45 ± 0.37	···	21 mJy at 31 GHz
Bolton et al. 2005 (9C follow-up)	1.4 to 4.8 GHz	124	···	0.44 [0.05, 0.76]	25 mJy at 15.2 GHz
Bolton et al. 2005 (9C follow-up)	4.8 to 15.2 GHz	124	···	0.39 [0.06, 0.95]	25 mJy at 15.2 GHz
Bolton et al. 2005 (9C follow-up)	15.2 to 43 GHz	124	···	0.87 [0.42, 1.20]	25 mJy at 15.2 GHz
Bolton et al. 2005 (9C follow-up)	1.4 to 4.8 GHz	70	···	0.24 [−0.12, 0.64]	60 mJy at 15.2 GHz
Bolton et al. 2005 (9C follow-up)	4.8 to 15.2 GHz	70	···	0.27 [0.02, 0.70]	60 mJy at 15.2 GHz
Bolton et al. 2005 (9C follow-up)	15.2 to 43 GHz	70	···	0.67 [0.38, 1.03]	60 mJy at 15.2 GHz

Table 4. Number counts for $\geq 5\sigma$ sources at 28.5 GHz.

log10(S) (mJy)	radius range (arcmin)[a]	raw counts	area (arcmin^2)	$log_{10}(dN/dS)$ (arcmin^{-2} mJy^{-1})	field type
$-0.15 : 0.00$	≥ 0.5	9	801	$-1.41^{+0.16}_{-0.17}$	cluster
$0.00 : 0.15$	≥ 0.5	7	1573	$-1.97^{+0.19}_{-0.20}$	cluster
$0.15 : 0.30$	≥ 0.5	11	2452	$-2.11^{+0.15}_{-0.15}$	cluster
$0.30 : 0.45$	≥ 0.5	6	3336	$-2.66^{+0.20}_{-0.22}$	cluster
$0.45 : 0.60$	≥ 0.5	8	4246	$-2.79^{+0.17}_{-0.18}$	cluster
$0.60 : 0.75$	≥ 0.5	9	5131	$-2.97^{+0.16}_{-0.17}$	cluster
$0.75 : 0.90$	≥ 0.5	6	5976	$-3.36^{+0.20}_{-0.22}$	cluster
$-0.20 : 0.10$	≤ 0.5	5	42.9	$-0.73^{+0.22}_{-0.25}$	cluster
$0.10 : 0.40$	≤ 0.5	7	63.5	$-1.06^{+0.19}_{-0.20}$	cluster
$0.40 : 0.70$	≤ 0.5	3	68.9	$-1.76^{+0.30}_{-0.34}$	cluster
$0.70 : 1.00$	≤ 0.5	2	69.6	$-2.24^{+0.37}_{-0.45}$	cluster
$0.10 : 0.50$	≥ 0.0	1	438	$-2.92^{+0.52}_{-0.76}$	non-cluster
$0.50 : 0.90$	≥ 0.0	1	745	$-3.55^{+0.52}_{-0.76}$	non-cluster

[a]Max radius varies for individual fields since set by noise. See text.

Table 5. Power law fits to dN/dS.

Field type	Best indiv. fit index	Best indiv. fit normalization	Best joint fit index	Best joint fit normalization
Inner cluster ($r \leq 0.5$ arcmin)	-1.74	$174^{+89}_{-39} \times 10^{-3}$ mJy^{-1} arcmin^{-2}	-1.98	$174^{+66}_{-48} \times 10^{-3}$ mJy^{-1} arcmin^{-2}
Outer cluster ($r \geq 0.5$ arcmin)	-2.02	$19.1^{+6.7}_{-4.9} \times 10^{-3}$ mJy^{-1} arcmin^{-2}	-1.98	$19.5^{+4.0}_{-5.0} \times 10^{-3}$ mJy^{-1} arcmin^{-2}
Non-cluster	...	...	-1.98	$5.81^{+6.70}_{-3.13} \times 10^{-3}$ mJy^{-1} arcmin^{-2}